Holographic Near-Field Microwave Imaging With Antenna Arrays in a Cylindrical Setup

Hailun Wu, *Member, IEEE*, Maryam Ravan, *Senior Member, IEEE*,
and Reza K. Amineh, *Senior Member, IEEE*

***Abstract*— Holographic microwave imaging is fast and robust and it has been adapted for near-field applications such as biomedical imaging and nondestructive testing. While the imaging technique is fast, synthesizing a 2-D aperture by mechanical scanning of the antennas takes time. Here, antenna arrays are used to expedite data acquisition along the azimuthal direction in a cylindrical holographic near-field microwave imaging setup. To deal with the limited and nonuniform samples along the azimuthal direction, three holographic imaging approaches are evaluated, in which, we use interpolation, uniform or nonuniform discrete Fourier transform (DFT), standardized low-resolution brain electromagnetic tomography (sLORETA), and exact low-resolution brain electromagnetic tomography (eLORETA). Besides, to make the system low-cost and portable, off-the-shelf components are used to construct a data acquisition system replacing the vector network analyzers. Simulation and experimental studies are conducted to validate the performance of the proposed imaging system. Structural similarity (SSIM) index is used to assess the quality of the reconstructed images.**

***Index Terms*— Antenna arrays, holography, microwave imaging, near-field imaging.**

I. INTRODUCTION

MICROWAVE imaging has been used in many applications due to the penetration of the electromagnetic waves at the corresponding frequencies inside many optically opaque materials. It has been used in concealed weapon detection (see [1]–[4]), nondestructive testing (see [5], [6]), biomedical imaging (see [7], [8]), and so on.

Microwave imaging techniques can be categorized into quantitative and qualitative techniques. Quantitative imaging seeks the exact dielectric property distributions by solving a nonlinear inverse scattering problem. Commonly, these approaches are ill-posed due to the insufficient amount of the acquired data. Besides, these techniques are time-consuming since they typically involve solving a complex and slow forward model for a large number of iterations in an optimization algorithm (see [9]). In contrast, qualitative imaging techniques have the potential to provide quasi real-time images of the inspected medium. This is accomplished using approximations such as linearization of the inverse scattering integral. Holographic techniques [3], [4], sensitivity-based techniques [10], [11], and confocal radar-based techniques [12], [13] are prominent approaches in this category. Since these techniques are typically fast and robust, they are growing rapidly in real-world applications. One mature application is millimeter-wave security screening of the passengers in the airports (see [3], [4], [14]–[16]) which is based on holographic processing. In [3] and [4], algorithms derived from the synthetic aperture radar (SAR) concepts provide 3-D images using wideband and complex-valued data scanned over rectangular and cylindrical apertures.

Recently, holographic imaging techniques have been extended to near-field applications, that is, where the imaged object is in the near-field of the antennas [17]. The main advantages of using near-field holographic imaging over SAR-based far-field holographic techniques are summarized here.

1) Far-field assumptions (analytic forms for the incident field and Green's function) limit the performance of SAR-based techniques to far-zone imaging. In near-field imaging applications, the imaging errors due to these assumptions might be less noticeable for large or high-contrast objects (see [18]) but more drastic for smaller or lower contrast objects (see [19]).
2) In SAR-based imaging, the wavenumbers along the cross-range and range directions are assumed to be independent variables and this leads to errors. In near-field holographic imaging techniques, this is not relevant (radial wavenumber is not introduced).
3) SAR-based far-field techniques, unlike the near-field holographic techniques, are incapable of processing the evanescent waves in the near-field applications. Thus, their resolution is diffraction-limited.
4) In SAR-based imaging, unlike near-field techniques, the antennas are assumed to be point-wise. Thus, the near-field components for the antennas are not taken into account.
5) SAR-based techniques work only based on the measurement of the backscattered waves, while the near-field holographic techniques can process backscattered and forward-scattered waves simultaneously.
6) In SAR-based techniques, wideband data are required for 3-D imaging, while near-field holographic techniques

---

Manuscript received July 11, 2020; revised October 2, 2020; accepted October 6, 2020. Date of publication October 30, 2020; date of current version January 5, 2021. This work was supported by the U.S. National Science Foundation (NSF) under Award 1920098 and in part by the New York Institute of Technology's Institutional Support for Research and Creativity (ISRC) Grants. *(Corresponding author: Reza K. Amineh.)*

The authors are with the Department of Electrical and Computer Engineering, New York Institute of Technology, New York, NY 10023 USA (e-mail: rkhalaja@nyit.edu).

Color versions of one or more of the figures in this article are available online at https://ieeexplore.ieee.org.

Digital Object Identifier 10.1109/TMTT.2020.3031897

have been proposed that accomplish 3-D imaging using narrowband data and arrays of receivers [20]–[22].

Holographic near-field imaging techniques have been developed for rectangular (see [23], [24]) and cylindrical (see [25]–[27]) setups. In particular, in [21], a low-cost and compact cylindrical system has been constructed using off-the-shelf components. There, to avoid the errors due to the dispersive properties of the media and to reduce the complexity of the data acquisition system, narrowband data are collected by an array of receiver antennas. The processing technique has been enhanced in [22] to alleviate the depth biasing problem using standardization of the solution. Although the image reconstruction is fast in [21] and [22], the data acquisition process is time-consuming due to the mechanical scanning of the antennas over a cylindrical aperture.

To expedite the data acquisition process, electronic scanning of antenna arrays can replace the mechanical scanning. One common approach is the use of the antenna arrays along one direction and mechanical scanning of the array along the orthogonal direction as proposed in [3], [4], and [28]. Also, in [29], a sparse multistatic linear antenna array has been proposed for sampling the scattered data which substantially reduces the number of antennas and switches. In [30], a microwave camera has been proposed that operates in the 20–30 GHz frequency range and it is capable of producing 3-D images at video frame rate. The processing technique is based on the SAR concepts. There, the dual-receiver design allows the use of antennas whose sizes are greater than half of the operating wavelength in an array configuration. In [31], an active E-band imager has been presented which measures in real-time. It is based on a stationary multistatic array architecture, and image reconstruction has been achieved based on a numerically optimized back-propagation algorithm. In [32], a microwave camera has been developed based on a 2-D array of switchable slot antennas. The data collection is based on the modulated scattering technique [33] and the processing is based on the SAR concepts.

In this article, we propose a cylindrical holographic near-field 3-D imaging system using arrays of the transmitter and receiver antennas. By replacing the conventional mechanical scanning along the azimuthal (ϕ) direction with the use of antenna arrays, data acquisition is faster. This is an important step that facilitates moving toward development of quasi real-time imaging systems. To deal with the limited (compared with mechanical scanning) and nonuniform samples along the azimuthal direction, three holographic imaging approaches are studied, in which we use interpolation, uniform or nonuniform discrete Fourier transform (DFT), standardized low-resolution electromagnetic tomography (sLORETA) [34] (as used in [22]), and exact low-resolution electromagnetic tomography (eLORETA) [35]. The images obtained from the proposed methods are compared using a quantitative measure. Besides, the low-cost, compact, and narrowband data acquisition system in [21] is extended further to perform the experiments.

II. THEORY OF HOLOGRAPHIC NEAR-FIELD 3-D IMAGING

In this section, we present the theory of holographic near-field imaging when using the data acquired by arrays of the transmitter and receiver antennas along the azimuthal direction. Fig. 1(a) illustrates the cylindrical microwave imaging system with the antenna arrays, and Fig. 1(b) shows the top view of the setup. N_T transmitter antennas with angular separation of $\Delta\phi_T$ are uniformly distributed covering the full circle. N'_R receiver antennas with angular separation of $\Delta\phi_R$ are uniformly placed in between every two transmitter antennas. This indicates that the antennas (regardless of being a transmitter or a receiver) are uniformly distributed over the aperture. The total number of the receivers is $N_R = N'_R \times N_T$ and the total number of the antennas is $N_A = N_R + N_T$. The antennas scan a cylindrical aperture with radius r_A and height z_A electronically along ϕ and mechanically along z (at multiple heights z_l, $l = 1, \ldots, N_z$) and at frequencies $\omega_{n_f}, n_f = 1, \ldots, N_f$. There are N_r cylindrical imaged surfaces at r_j, $j = 1, \ldots, N_r$.

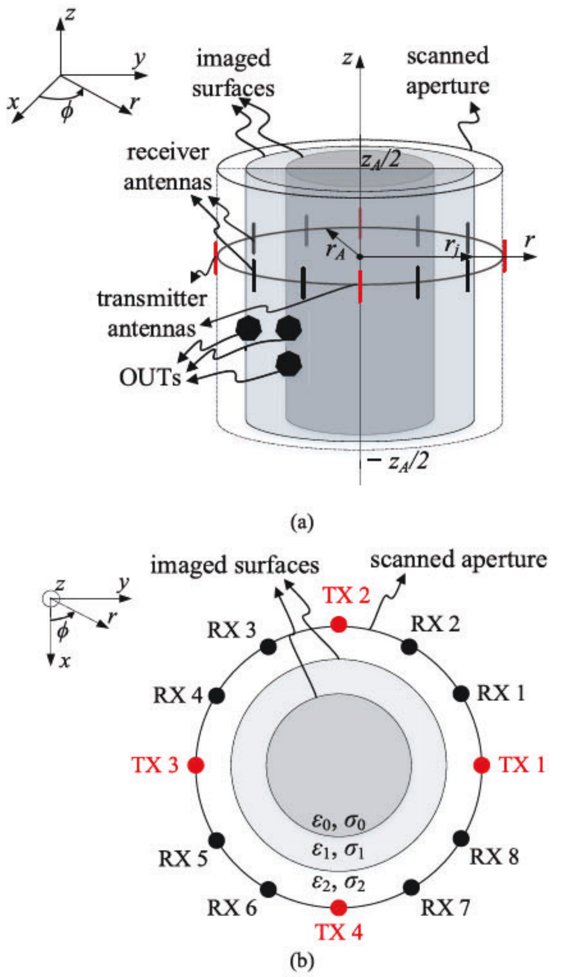

(a)

(b)

Fig. 1. (a) Proposed cylindrical imaging setup and (b) top view of the setup (ε_j and σ_j, $j = 0, \ldots, N_r$ denote the electrical permittivities and conductivities of the media, respectively). TX and RX stand for the transmitter and receiver antennas, respectively.

First, the scattered responses $E^{SC,CO}_{j,a_m}(\phi_{k'}, z_l, \omega_{n_f})$ due to small calibration objects (COs) placed at the cylindrical coordinates (r, ϕ, z) of $(r_j, 0, 0)$, one at a time, illuminated by each transmitter a_m and received by all receivers at azimuthal angles $\phi_{k'}$, are recorded where $k' = 1, \ldots, N_R$. The imaging system is assumed to be linear and space-invariant (LSI). The scattered responses $E^{SC,CO}_{j,a_m}(\phi_{k'}, z_l, \omega_{n_f})$ approximate the point-spread functions (PSFs) for such system (see [21], [22]).

Then, the complex-valued scattered field $E^{SC}_{a_m}(\phi_{k'}, z_l, \omega_{n_f})$ with the presence of the objects under test (OUTs) illuminated by each transmitter a_m and received by the receivers at azimuthal angles $\phi_{k'}$ are recorded. In the following, we present three methods for processing the data acquired by this setup.

A. Method 1: Use of Interpolation, Uniform DFT, and sLORETA

In Method 1, once all $E^{SC,CO}_{j,a_m}(\phi_{k'}, z_l, \omega_{n_f})$ and $E^{SC}_{a_m}(\phi_{k'}, z_l, \omega_{n_f})$ responses are collected, interpolation is used to obtain responses $E^{SC,CO}_{j,a_m}(\phi_k, z_l, \omega_{n_f})$ and $E^{SC}_{a_m}(\phi_k, z_l, \omega_{n_f})$ in which ϕ_k angles are uniformly distributed over a full circle at each height z_l. Then, $E^{SC}_{a_m}(\phi_k, z_l, \omega_{n_f})$ can be written as the sum of the convolutions of the PSF for each surface $E^{SC,CO}_{j,a_m}(\phi_k, z_l, \omega_{n_f})$ with the contrast function of the OUTs for the corresponding surface $f_j(\phi_k, z_l)$ as [21], [22]

$$E^{SC}_{a_m}(\phi_k, z_l, \omega_{n_f}) = \sum_{j=1}^{Nr} E^{SC,CO}_{j,a_m}(\phi_k, z_l, \omega_{n_f}) *_\phi *_z f_j(\phi_k, z_l) \tag{1}$$

where $*_\phi$ and $*_z$ denote the convolutions along the ϕ- and z-directions, respectively. Writing (1) at all N_f frequencies and N_T transmitters and applying discrete-time Fourier transform (DTFT) and DFT to both sides of the equations along the z- and ϕ-directions, respectively, leads to the following system of equations at each spatial frequency pair $\boldsymbol{\kappa} = (k_\phi, k_z)$ (k_ϕ and k_z are the Fourier variables corresponding to ϕ and z, respectively) [22]:

$$\underline{\tilde{\tilde{\mathbf{E}}}}^{SC}_{(N_T N_f \times 1)} = \underline{\underline{\tilde{\tilde{\mathbf{D}}}}}_{(N_T N_f \times N_r)} \underline{\tilde{\tilde{\mathbf{F}}}}_{(N_r \times 1)} \tag{2}$$

where

$$\underline{\tilde{\tilde{\mathbf{E}}}}^{SC} = \underline{\mathbf{L}} \begin{bmatrix} \underline{\tilde{\tilde{\mathbf{E}}}}^{SC}_1 \\ \vdots \\ \underline{\tilde{\tilde{\mathbf{E}}}}^{SC}_{N_T} \end{bmatrix}, \quad \underline{\underline{\tilde{\tilde{\mathbf{D}}}}} = \mathbf{L} \begin{bmatrix} \underline{\underline{\tilde{\tilde{\mathbf{D}}}}}_1 \\ \vdots \\ \underline{\underline{\tilde{\tilde{\mathbf{D}}}}}_{N_T} \end{bmatrix}, \quad \underline{\tilde{\tilde{\mathbf{F}}}} = \begin{bmatrix} \tilde{\tilde{f}}_1(\boldsymbol{\kappa}) \\ \vdots \\ \tilde{\tilde{f}}_{N_r}(\boldsymbol{\kappa}) \end{bmatrix} \tag{3}$$

and

$$\underline{\tilde{\tilde{\mathbf{E}}}}^{SC}_{a_m(N_f \times 1)} = \begin{bmatrix} \tilde{\tilde{E}}^{SC}_{a_m}(\boldsymbol{\kappa}, \omega_1) \\ \vdots \\ \tilde{\tilde{E}}^{SC}_{a_m}(\boldsymbol{\kappa}, \omega_{N_f}) \end{bmatrix} \tag{4}$$

$$\underline{\underline{\tilde{\tilde{\mathbf{D}}}}}_{a_m(N_f \times N_r)} = \begin{bmatrix} \tilde{\tilde{E}}^{SC,CO}_{1,a_m}(\boldsymbol{\kappa}, \omega_1) & \cdots & \tilde{\tilde{E}}^{SC,CO}_{N_r,a_m}(\boldsymbol{\kappa}, \omega_1) \\ \vdots & \ddots & \vdots \\ \tilde{\tilde{E}}^{SC,CO}_{1,a_m}(\boldsymbol{\kappa}, \omega_{N_f}) & \cdots & \tilde{\tilde{E}}^{SC,CO}_{N_r,a_m}(\boldsymbol{\kappa}, \omega_{N_f}) \end{bmatrix} \tag{5}$$

where $\tilde{\tilde{E}}^{SC}_{a_m}(\boldsymbol{\kappa}, \omega_{n_f})$, $\tilde{\tilde{E}}^{SC,CO}_{j,a_m}(\boldsymbol{\kappa}, \omega_{n_f})$, and $\tilde{\tilde{f}}_j(\boldsymbol{\kappa})$ are obtained by taking DFT along ϕ and DTFT along z of $E^{SC}_{a_m}(\phi_k, z_l, \omega_{n_f})$, $E^{SC,CO}_{j,a_m}(\phi_k, z_l, \omega_{n_f})$, and $f_j(\phi_k, z_l)$, respectively, $\underline{\underline{\mathbf{L}}}_{(N_f N_T \times N_f N_T)} = \underline{\underline{\mathbf{I}}} - \underline{\mathbf{1}}\,\underline{\mathbf{1}}^{\mathrm{T}} / \underline{\mathbf{1}}^{\mathrm{T}} \underline{\mathbf{1}}$ denotes the centering matrix that is the average reference operator, $\underline{\underline{\mathbf{I}}}_{(N_f N_T \times N_f N_T)}$ is the identity matrix, and $\underline{\mathbf{1}}_{(N_f N_T \times 1)}$ is a vector of ones. The centering matrix $\underline{\underline{\mathbf{L}}}$ is a symmetric and idempotent matrix, which when multiplied with a vector (or columns of a matrix) has the same effect as subtracting the mean of the components of the vector from every component of that vector.

The system of equations in (2) is solved at each $\boldsymbol{\kappa} = (k_\phi, k_z)$ pair to obtain the values for $\tilde{\tilde{f}}_j(\boldsymbol{\kappa})$, $j = 1, \ldots, N_r$. Then, inverse DTFT along z and inverse DFT along ϕ are applied to reconstruct images $f_j(\phi_k, z_l)$ over all the imaged surfaces. At the end, the normalized modulus of $f_j(\phi_k, z_l)$, $|f_j(\phi_k, z_l)|/M$, where M is the maximum of $|f_j(\phi_k, z_l)|$ for all r_j, is plotted to obtain a 2-D image of the OUTs at each surface $r = r_j$. We call $|f_j(\phi_k, z_l)|/M$ the normalized image.

It has been shown in [22] that the use of the sLORETA approach [34] to solve the system of equations in (2), when the data are provided by an array of receiver antennas, leads to significantly higher quality images compared with the conventionally used minimum norm (MN) approach. MN solutions are biased toward superficial objects because of their spatial vicinity to the antennas. The use of the sLORETA approach alleviates the depth biasing problem associated with the MN approach even in the presence of measurement noise by standardization of the solution. In the sLORETA approach, the standardized solution $\widehat{\underline{\tilde{\tilde{\mathbf{F}}}}}$ is written as

$$\widehat{\underline{\tilde{\tilde{\mathbf{F}}}}} = \sqrt{(\mathrm{Diag}(\underline{\underline{\mathbf{S}}}_{\tilde{\tilde{\mathbf{F}}}}))^{-1}} \underline{\underline{\mathbf{P}}}\, \underline{\tilde{\tilde{\mathbf{E}}}}^{SC} \tag{6}$$

where $\underline{\underline{\mathbf{S}}}_{\tilde{\tilde{\mathbf{F}}}(N_r \times N_r)}$ is the variance of $\underline{\tilde{\tilde{\mathbf{F}}}}$ and it can be obtained from

$$\underline{\underline{\mathbf{S}}}_{\tilde{\tilde{\mathbf{F}}}} = \underline{\underline{\mathbf{P}}} \mathbf{S}_{\tilde{\tilde{\mathbf{E}}}^{SC}} \underline{\underline{\mathbf{P}}}^H. \tag{7}$$

$\underline{\underline{\mathbf{S}}}_{\tilde{\tilde{\mathbf{E}}}^{SC}(N_T N_f \times N_T N_f)}$ is the variance of $\underline{\tilde{\tilde{\mathbf{E}}}}^{SC}$ from the Bayesian point of view, $\mathrm{Diag}(\underline{\underline{\mathbf{S}}}_{\tilde{\tilde{\mathbf{F}}}})$ is the diagonal matrix formed by the diagonal elements of $\underline{\underline{\mathbf{S}}}_{\tilde{\tilde{\mathbf{F}}}}$, and $\underline{\underline{\mathbf{P}}}_{(N_r \times N_T N_f)}$ is obtained from

$$\underline{\underline{\mathbf{P}}} = \underline{\underline{\tilde{\tilde{\mathbf{D}}}}}^H \left[\underline{\underline{\tilde{\tilde{\mathbf{D}}}}}\, \underline{\underline{\tilde{\tilde{\mathbf{D}}}}}^H + \alpha \underline{\underline{\mathbf{L}}} \right]^+ \tag{8}$$

where $[\cdot]^H$ is the Hermitian transpose operation, and $[\cdot]^+$ denotes the Moore–Penrose pseudoinverse. Also, α is a regularization parameter and it is taken as the variance of the noise in the simulated or measured data. Here, we estimate the noise variance by minimizing the generalized cross-validation (GCV) score [36] using MATLAB command *evar*. In this method, it is assumed that the value for which the GCV score is minimal can provide the variance of the additive noise.

B. Method 2: Use of Interpolation, Uniform DFT, and eLORETA

In Method 2, again, the irregular samples along the ϕ-direction are first interpolated to provide uniform samples along that direction. Then, similar to Section II-A, the systems of equations in (2) at $\boldsymbol{\kappa} = (k_\phi, k_z)$ pairs are constructed. Here, we propose solving the systems of equations using the eLORETA approach [35] which is a genuine inverse solution (not merely a linear imaging method) with exact, zero error localization in the presence of measurement and structured noise.

To implement eLORETA, consider the general weighted MN problem [37]

$$\min_{\underline{\tilde{\tilde{\mathbf{F}}}}}\left[\left\|\underline{\tilde{\tilde{\mathbf{E}}}}^{SC}-\underline{\underline{\tilde{\tilde{\mathbf{D}}}}}\,\underline{\tilde{\tilde{F}}}\right\|^2+\alpha\underline{\tilde{\tilde{\mathbf{F}}}}^H\,\underline{\underline{\mathbf{W}}}\underline{\tilde{\tilde{\mathbf{F}}}}\right] \tag{9}$$

where $\underline{\underline{\mathbf{W}}}_{N_r\times N_r}$ denotes the symmetric weight matrix and $\alpha\geq 0$ denotes the regularization parameter. The estimated solution is linear as

$$\underline{\widehat{\tilde{\tilde{\mathbf{F}}}}}=\underline{\underline{\mathbf{Q}}}\underline{\tilde{\tilde{\mathbf{E}}}}^{SC} \tag{10}$$

where

$$\underline{\underline{\mathbf{Q}}}_{(N_r\times N_T N_f)}=\underline{\underline{\mathbf{W}}}^{-1}\underline{\underline{\tilde{\tilde{\mathbf{D}}}}}^H\left[\underline{\underline{\tilde{\tilde{\mathbf{D}}}}}\,\underline{\underline{\mathbf{W}}}^{-1}\,\underline{\underline{\tilde{\tilde{\mathbf{D}}}}}^H+\alpha\underline{\underline{\mathbf{L}}}\right]^+ \tag{11}$$

$\alpha\underline{\underline{\mathbf{L}}}$ is the covariance matrix of the measurement noise, and $\underline{\underline{\mathbf{W}}}^{-1}_{N_r\times N_r}$ is *a priori* covariance matrix for $\underline{\tilde{\tilde{\mathbf{F}}}}$.

By extending linear relation in (2) to include possible additive measurement noise and assuming independence of $\underline{\tilde{\tilde{\mathbf{F}}}}$ and measurement noise, the covariance matrix for $\underline{\tilde{\tilde{\mathbf{E}}}}^{SC}$ can be written as

$$\operatorname{cov}(\underline{\tilde{\tilde{E}}}^{SC})=\underline{\underline{\tilde{\tilde{\mathbf{D}}}}}\,\underline{\underline{\mathbf{W}}}^{-1}\,\underline{\underline{\tilde{\tilde{\mathbf{D}}}}}^H+\alpha\underline{\underline{\mathbf{L}}}. \tag{12}$$

Based on the linear relation in (10), the covariance matrix for $\underline{\widehat{\tilde{\tilde{\mathbf{F}}}}}$ is

$$\operatorname{cov}(\underline{\widehat{\tilde{\tilde{\mathbf{F}}}}})=\underline{\underline{\mathbf{W}}}^{-1}\,\underline{\underline{\tilde{\tilde{\mathbf{D}}}}}^H(\underline{\underline{\tilde{\tilde{\mathbf{D}}}}}\,\underline{\underline{\mathbf{W}}}^{-1}\,\underline{\underline{\tilde{\tilde{\mathbf{D}}}}}^H+\alpha\underline{\underline{\mathbf{L}}})^+\,\underline{\underline{\tilde{\tilde{\mathbf{D}}}}}\,\underline{\underline{\mathbf{W}}}^{-1}. \tag{13}$$

When $\underline{\underline{\mathbf{W}}}$ is restricted to be a diagonal matrix, then the solution to the problem

$$\begin{aligned}&\min_{\underline{\underline{\mathbf{W}}}}\left\|\underline{\underline{\mathbf{I}}}-\operatorname{cov}(\underline{\widehat{\tilde{\tilde{\mathbf{F}}}}})\right\|^2\\&=\min_{\underline{\underline{\mathbf{W}}}}\left\|\underline{\underline{\mathbf{I}}}-\underline{\underline{\mathbf{W}}}^{-1}\,\underline{\underline{\tilde{\tilde{\mathbf{D}}}}}^H(\underline{\underline{\tilde{\tilde{\mathbf{D}}}}}\,\underline{\underline{\mathbf{W}}}^{-1}\,\underline{\underline{\tilde{\tilde{\mathbf{D}}}}}^H+\alpha\underline{\underline{\mathbf{L}}})^+\,\underline{\underline{\tilde{\tilde{\mathbf{D}}}}}\,\underline{\underline{\mathbf{W}}}^{-1}\right\|^2\end{aligned} \tag{14}$$

produces an inverse solution (10) with zero localization error. The following iterative algorithm converges to the diagonal weights $\underline{\underline{\mathbf{W}}}$ that solve the problem in (14) [35].

1) Given $\underline{\underline{\tilde{\tilde{\mathbf{D}}}}}$ and a regularization parameter α, initialize the diagonal weight matrix $\underline{\underline{\mathbf{W}}}$ as the identity matrix.

2) Set

$$\underline{\underline{\mathbf{M}}}_{(N_f N_T\times N_f N_T)}=(\underline{\underline{\tilde{\tilde{\mathbf{D}}}}}\,\underline{\underline{\mathbf{W}}}^{-1}\,\underline{\underline{\tilde{\tilde{\mathbf{D}}}}}^H+\alpha\underline{\underline{\mathbf{L}}})^+. \tag{15}$$

3) For $i=1$ to N_r

$$\underline{\underline{\mathbf{W}}}(i,i)=\sqrt{(\underline{\underline{\tilde{\tilde{\mathbf{D}}}}}^H\,\underline{\underline{\mathbf{M}}}\,\underline{\underline{\tilde{\tilde{\mathbf{D}}}}})}. \tag{16}$$

4) Go to step 2 until convergence is reached based on the negligible changes in $\underline{\underline{\mathbf{W}}}$.

Finally, the diagonal matrix $\underline{\underline{\mathbf{W}}}$ produced by this algorithm is used to provide matrix $\underline{\underline{\mathbf{Q}}}$ in (11) and, therefore, the estimated solution $\underline{\widehat{\tilde{\tilde{\mathbf{F}}}}}$ in (10).

It has been shown in [35] that eLORETA is unbiased in the presence of structured noise for $\underline{\tilde{\tilde{\mathbf{F}}}}$ with covariance matrix of the form $\underline{\underline{\mathbf{W}}}^{-1}$. Unfortunately, such a structure for noise of $\underline{\tilde{\tilde{\mathbf{F}}}}$ may not hold in practice. This can be considered as a disadvantage of eLORETA compared with sLORETA.

C. Method 3: Use of Nonuniform DFT, sLORETA, and Interpolation

In Method 3, unlike Methods 1 and 2, data are not interpolated prior to taking DFT along the ϕ-direction. Instead, the nonuniform samples along ϕ are transformed using a nonlinear DFT (NUDFT). Then, the construction of the systems of equations and the solution of them using sLORETA is similar to those steps described for Method 1.

Once all the systems of equations are solved, the process of forming the normalized images is similar to that in Method 1 except that inverse NUDFT is applied along the ϕ-direction in the image reconstruction process and, at the end, interpolation is applied along the ϕ-direction. The latter step is implemented to enhance the quality of the images (increase the number of pixels along ϕ) and compare the images for the three methods. A review of NUDFT and inverse NUDFT processing has been provided in Appendix A.

III. SIMULATION RESULTS

First, we assess the performance of the proposed imaging techniques via FEKO simulations. The study is performed by simulating responses at 5 frequencies within a band of 0.4 GHz around a center frequency of 1.7 GHz. To have a realistic study of the performance of the imaging technique, White Gaussian noise is added to the simulated data with a signal-to-noise ratio (SNR) of 20 dB. Besides, to assess the quality of the reconstructed images, we use the structural similarity (SSIM) index [38]. Please refer to Appendix B for details of computing SSIM. Here, SSIM is computed for each reconstructed 2-D image when taking the true OUTs' image as the reference. The true image has a value of 1 at the pixels overlapping the OUTs and 0 elsewhere. Higher SSIM values indicate higher similarity to the true image.

A. Imaging Objects in a Uniform Background Medium

For the examples in this section, the background medium has properties of $\varepsilon_r=22$ and $\sigma=1.25$ S/m. The scattered data for the imaged OUTs are collected over a cylindrical aperture with $r_A=68$ mm and $z_A=376$ mm (10λ, where λ is the wavelength at 1.7 GHz for the medium). The antennas are resonant ($\lambda/2$) dipoles. The sampling step along the z-direction is $\Delta z=17.9$ mm ($\lambda/2$). The angular separation between transmitter antennas is $\Delta\phi_T=40°$. The angular separation between adjacent receiver antennas is $\Delta\phi_R=10°$(no receiver antennas at the position of transmitters). This indicates that there are nine transmitter antennas and 27 receiver antennas.

The cylindrical imaged surfaces are at $r_j=50$, 32, and 14 mm. Thus, to collect PSF data, we place cuboids with a size of 5 mm at the cylindrical coordinates (r,ϕ,z) of $(r_j,0°,0)$, one at a time, and simulate the responses.

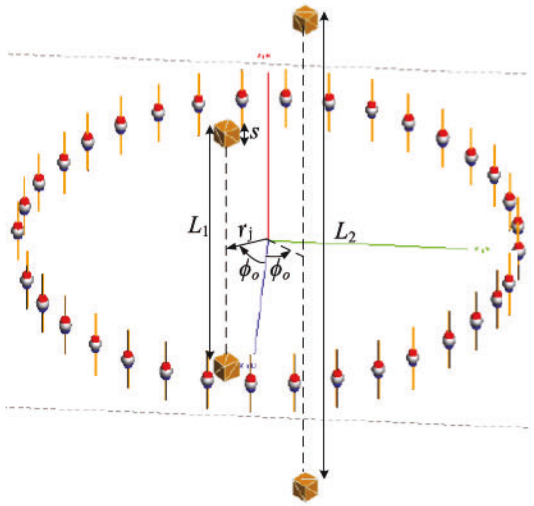

Fig. 2. FEKO simulation model for the first example.

TABLE I

VALUES OF THE PARAMETERS FOR THE FIRST SIMULATION EXAMPLE

N_A	r_A	$\Delta\phi_T$	$\Delta\phi_R$	S	ϕ_o	L_1	L_2
36	68 mm	40°	10°	5 mm	50°	λ	2λ

TABLE II

VALUES OF THE PARAMETERS FOR THE SECOND SIMULATION EXAMPLE

N_A	r_A	$\Delta\phi_T$	$\Delta\phi_R$	S	ϕ_o	w	L
36	68 mm	40°	10°	5 mm	50°	$\lambda/4$	2λ

First, we perform the simulation study when four perfect electric conductor (PEC) cuboids are placed on the cylindrical surface of $r_3 = 14$ mm as shown in Fig. 2. Table I shows the values of the parameters for this example. Fig. 3 shows the reconstructed images when implementing Methods 1 to 3. To implement Method 1, the data acquired from 27 receiver antennas are interpolated along the ϕ-direction to obtain 144 samples uniformly covering 0° to360° (every 2.5°). The interpolation is implemented in MATLAB using *interp1* command and the shape-preserving piecewise cubic interpolation. To implement Method 3, the final images are interpolated similarly to obtain 144 samples along ϕ uniformly covering 0° to 360°. From Fig. 3, it is observed that the images obtained from Method 1 have the best quality, correctly reconstructing the objects. The images obtained from Method 2 have comparable but slightly lower quality compared with those for Method 1. The images for Method 3 show the worst quality for the reconstructed objects.

Next, to study the shape reconstruction capability of the methods, we simulate the responses for a cross-shaped PEC object. Fig. 4 shows the simulation model for this example and Table II shows the values of the parameters. The object is placed at $r_2 = 32$ mm surface. The images are reconstructed over surfaces with radii similar to those in the first example. Fig. 5 shows the reconstructed images when implementing Methods 1 to 3. The images obtained from Methods 1 and 2 have very similar quality with close SSIM values. The shape of the object on the middle surface is reconstructed with the arm along the z-axis having higher contrast since the dipole antennas are z-polarized. The images at the inner surface ($r_3 = 14$ mm) show higher levels of artifacts compared with the images at the outer surface ($r_1 = 50$ mm). The images obtained from Method 3 have the worst quality and the lowest SSIM values except for the image at $r_1 = 50$ mm which does not contain the object.

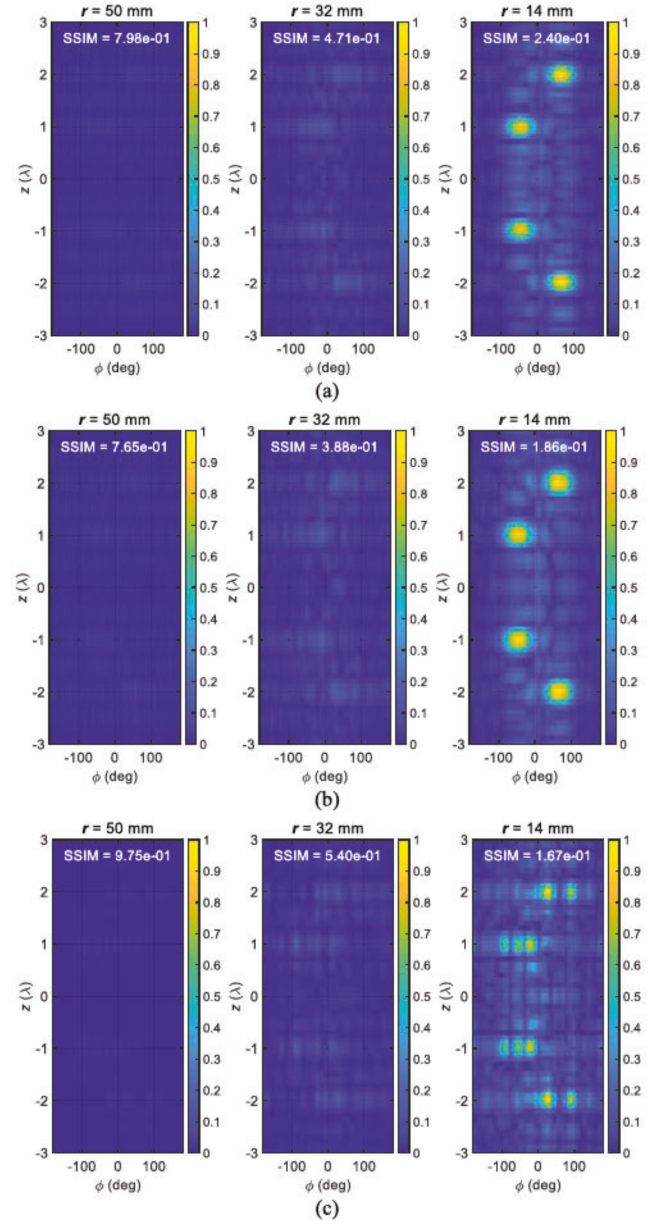

(a)

(b)

(c)

Fig. 3. Normalized images of the first simulation example for (a) Method 1, (b) Method 2, and (c) Method 3.

In general, from the studied examples, we conclude that Methods 1 and 2 have similar performance and they offer better imaging quality compared with Method 3. Thus, in the following, we study the resolutions for Method 1.

The cross-range resolution along z (δz) is estimated from images of the COs over each surface. For this purpose,

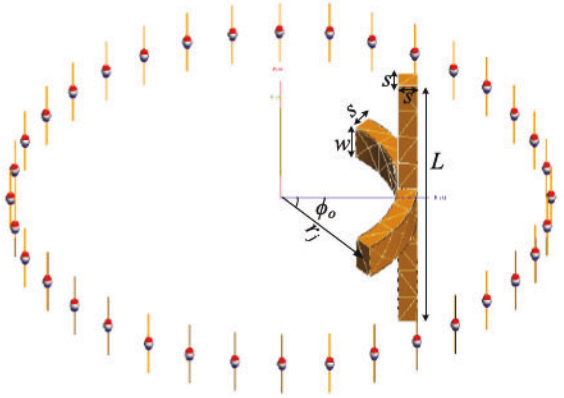

Fig. 4. FEKO simulation model for the second example.

we measure the distance between two points marking 0.7 times the peak value for the image of the CO. The estimated values for δz on the outer, middle, and inner surfaces are approximately 10.7 mm (0.28λ), 10.7 mm (0.28λ), and 14.3 mm (0.38λ), respectively.

Similarly, the cross-range resolution along ϕ ($\delta\phi$ in radian) is defined as the angular width between two points marking 0.7 times the peak value for the image of the CO. The estimated values for $\delta\phi$ on the outer, middle, and inner surfaces are 0.11, 0.35, and 0.77 rad, respectively.

To evaluate the range resolution, we image a CO when it is placed at $r_2 = 32$ mm. We implement the imaging process when the radial distance between the three imaged surfaces varies, while the radial position of the middle surface is kept fixed at 32 mm. We determine the range resolution as the radial distance between the inner and outer imaged surfaces for which the value of the image is 0.7 (while the maximum level of the object's image over the middle plane has a value of 1 due to normalization). This leads to a range resolution δr of approximately 22 mm.

Please note that in general in this near-field imaging technique, resolution limits highly depend on the position, type, and electric properties of the objects, the antenna structure, the dielectric properties of the background medium, the dimensions of the scanned aperture, and the SNR values for the responses.

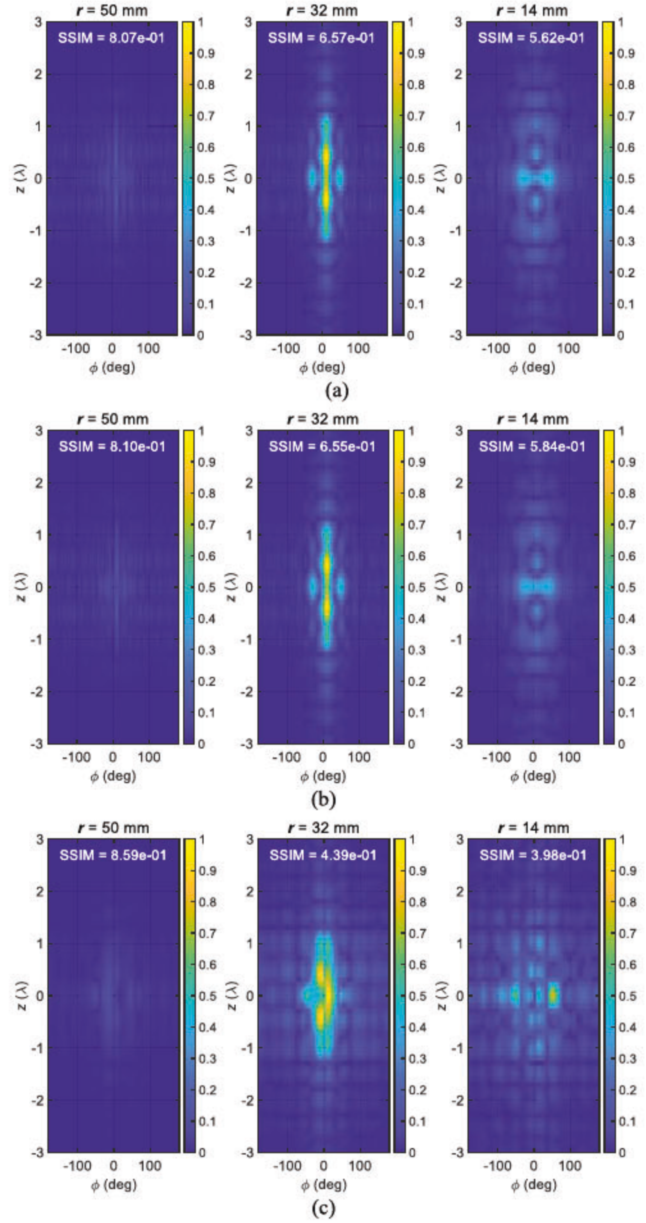

Fig. 5. Normalized images of the second simulation example for (a) Method 1, (b) Method 2, and (c) Method 3.

B. Imaging Objects Hidden Inside a Cylindrical Host Medium

As a third simulation example, we present the imaging results for a setup similar to the one used later in the experiments. Fig. 6 shows this setup, in which a cylindrical host medium has properties of $\varepsilon_r = 22$ and $\sigma = 1.25$ S/m. The antennas are resonant dipoles at 1.7 GHz and surround this medium in the air. To reduce the coupling between the antennas, microwave-absorbing sheets (absorbers) made of carbon fibers with properties of $\varepsilon_r = 4.54$ and $\sigma = 55000$ S/m are placed in between the antennas. The number and angular separation of the antennas are similar to the previous examples. The synthesized aperture has a length of 150 mm and 21 samples along the z-axis. The hidden objects are two PEC cylinders with diameter of 18 mm and height of 50 mm centered at the cylindrical coordinates (r, ϕ, z) of (20 mm, 0°, 0) and (20 mm, −170°, 0) and aligned along the z-axis. The cylindrical imaged surfaces are at $r_j = 50$, 35, and 20 mm. Thus, to collect PSF data, we place cylindrical PEC objects with diameter of 18 mm and height of 10 mm at the cylindrical coordinates (r, ϕ, z) of $(r_j, 0, 0)$, one at a time, and measure the responses.

Fig. 7(a) shows the reconstructed images for this example. It is observed that the two hidden objects can be reconstructed well. The coupling between two adjacent antennas is almost −6 and −14 dB without and with the use of microwave absorbers, respectively. To study the effect of using microwave absorbers, we perform imaging for the same setup but without microwave absorbers. Fig. 7(b) shows the images for this case.

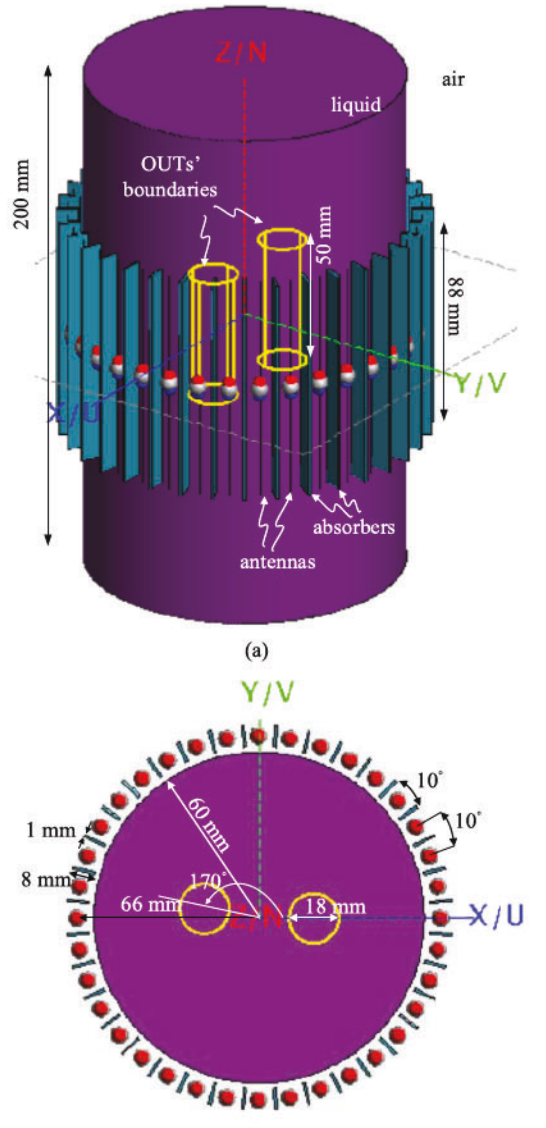

(a)

(b)

Fig. 6. FEKO simulation model for the third example with parameter values similar to the measurement setup. (a) Isometric view. (b) Top view.

It is clear that the quality of the reconstructed image of the OUTs is lower compared with that in Fig. 7(a).

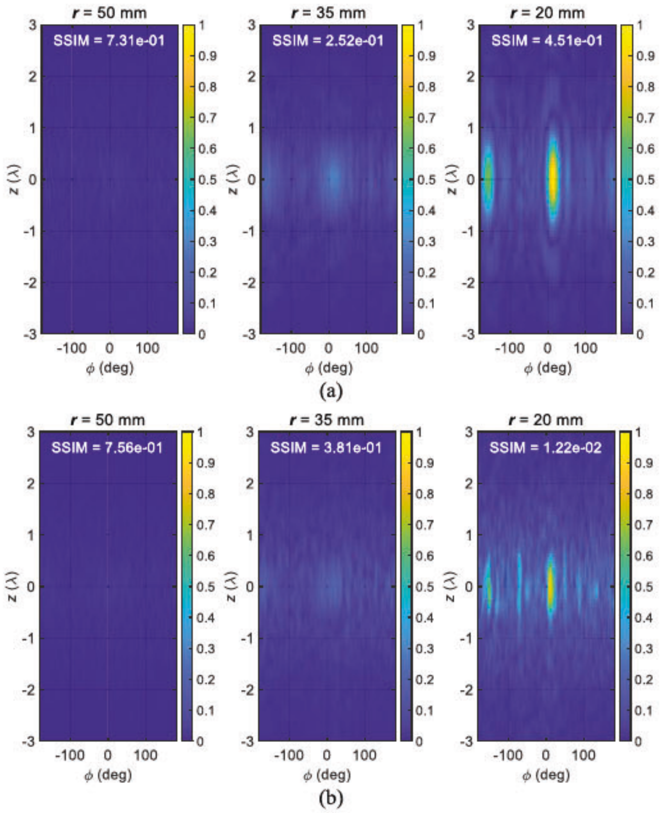

(a)

(b)

Fig. 7. Normalized images for the third simulation example using Method 1 (a) with microwave absorbers and (b) without microwave absorbers.

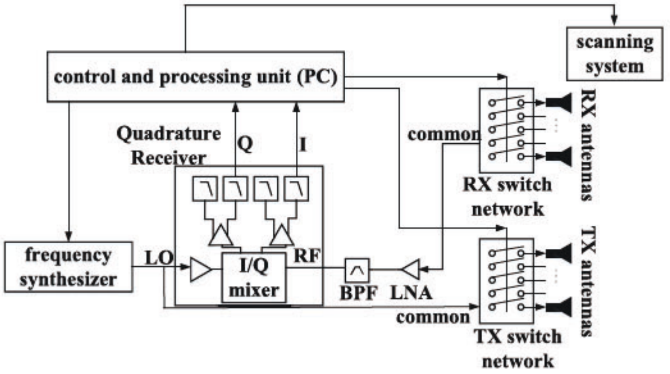

Fig. 8. Block diagram of the imaging system.

IV. DATA ACQUISITION SYSTEM

Fig. 8 shows the block diagram of the proposed data acquisition system which is an extended version of the one in [21]. It consists of microwave circuits to transmit and receive signals, an array of transmitter antennas, an array of receiver antennas, two switching networks for selecting transmitters and receivers, a control and processing unit, and a cylindrical scanning system. The transmitted signal is generated by a frequency synthesizer controlled by the control and processing unit. The frequency synthesizer also provides local (LO) signal for the quadrature receiver. The received signal passes a low-noise amplifier (LNA) and a bandpass filter (BPF) before reaching the direct conversion (homodyne) quadrature receiver. The quadrature receiver provides in-phase (I) and quadrature (Q) outputs to the processing unit.

Fig. 9 shows the imaging system with its main components zoomed in. For better illustration, please refer to Fig. 6 which shows an imaging system with parameters similar to the one used in the experiments (it does not include the antenna array holder). In the setup, a container with diameter of 120 mm and height of 200 mm is filled with a mixture of 20% water and 80% glycerin with properties of $\varepsilon_r = 22$ and $\sigma = 1.25$ S/m within the frequency band of 1.5−1.9 GHz [39]. The OUTs are plastic cylinders with diameter of 18 mm and height of 50 mm covered by thin copper sheets and placed inside the liquid container. The scanning system moves the

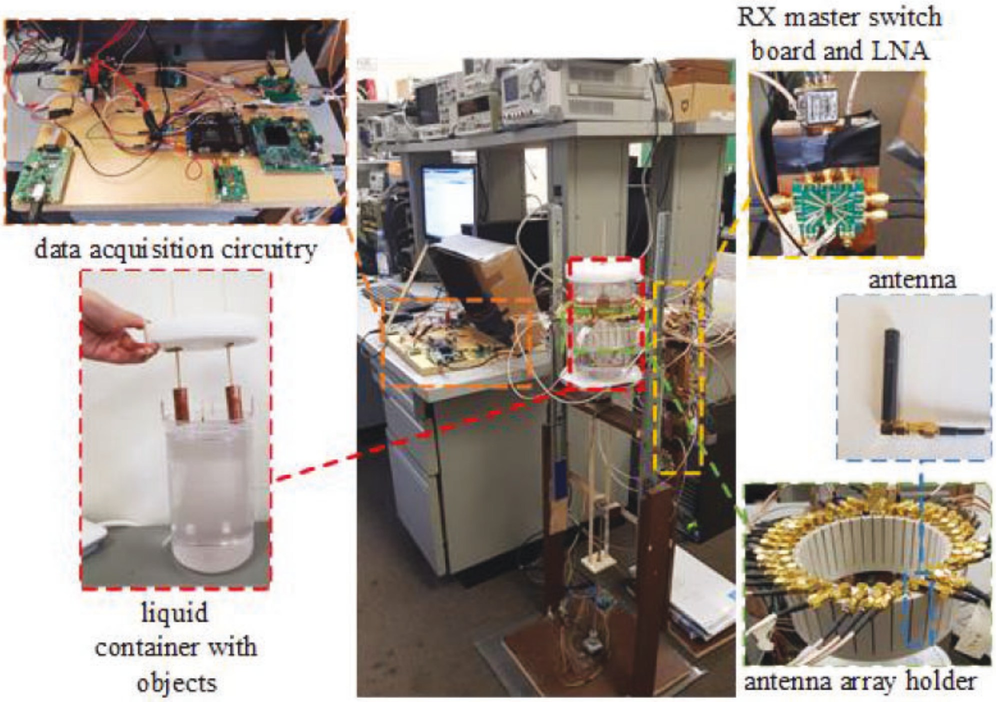

Fig. 9. Imaging system with its main components zoomed in.

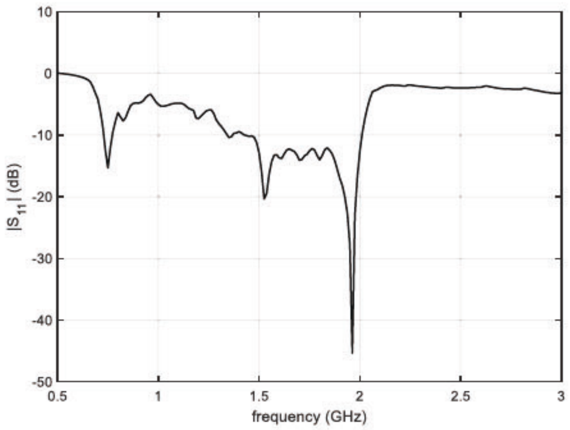

Fig. 10. Measured $|S_{11}|$ for one sample antenna when it is placed inside the antenna array holder with the presence of the liquid container.

liquid container along the longitudinal direction (z) and it includes an Arduino Uno board, an Arduino motor shield board, and a stepper motor. The antenna arrays are stationary and placed inside a customized holder made by 3-D printing and tightly in contact with the liquid container. The antenna arrays consist of 36 antennas, 9 of them operating as transmitters and the remaining as receivers. The array elements are mini GSM/Cellular Quad-Band antennas from Adafruit Company. Microwave-absorbing sheets are placed in 36 slots with a width of 1 mm which are cut out of the antenna holder to reduce the coupling between the antennas.

Fig. 10 shows the measured $|S_{11}|$ for one sample antenna when it is placed inside the customized antenna array holder with the presence of the liquid container. The value of $|S_{11}|$ is mostly below -10 dB over the targeted frequency band of 1.5$-$1.9 GHz.

The details of the transmitter and receiver modules can be found in [21]. Here, two separate switching networks for the transmitter and receiver antenna arrays are added using Arduino Uno boards and EV1HMC321ALP4E modules which are RF SP8T switches from Analog Devices. The switching network for the transmitter array consists of one Arduino Uno board and two RF SP8T switch modules: a master module and a slave module. These switch modules are controlled by MATLAB via the Arduino Uno board. A similar switching network is developed for selecting the receiver antennas. This network consists of one Arduino Uno board and four RF SP8T switch modules, a master module, and three slave modules, and it is controlled by MATLAB via another Arduino Uno board.

Fig. 11 shows the transmitted signal power versus frequency right after VGA and for three control voltages for the VGA. It is observed that the transmitted power decreases with the increase in frequency. Fig. 12 shows the received signal power versus frequency after LNA and BPF and before entering the quadrature receiver module for a sample transmitter–receiver pair with the maximum possible distance between them (approximately 130 mm) and for three values of control voltages of the VGA. The power of the received signal follows the same trend as those shown in Fig. 11. Besides, the power of the received signal is much lower compared with the transmitted signal due to the attenuation inside the lossy mixture of water and glycerin. According to the manufacturer, the receiver unit (DC1513B-AB) has the following

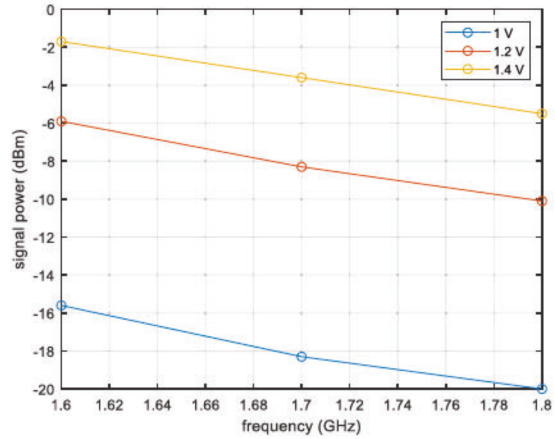

Fig. 11. Transmitted signal power versus frequency right after VGA and for three values of control voltages for the VGA.

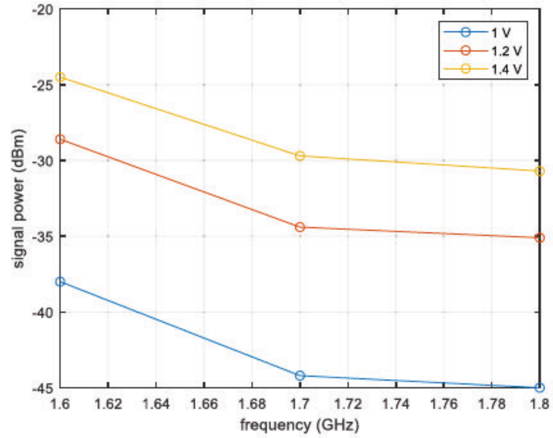

Fig. 12. Received signal power versus frequency after LNA and BPF and before quadrature receiver module for a sample transmitter–receiver antenna pair with the maximum possible distance between them (approximately 130 mm). This is plotted for three values of control voltages of the VGA.

specifications: maximum RF input of 20 dBm and dynamic range of 95 dBm. This implies that the received power needs to be above −75 dBm to be detectable by the receiver unit. Thus, even with the control voltage of 1 V for the VGA and the largest possible distance between the transmitter and receiver antennas, the received signal is still detectable. To have the strongest received signal, we set the VGA control voltage to 1.4 V in the experiments.

V. Experimental Results

Here, the performance of the proposed imaging system is studied via experiments. The operation frequency is from 1.5 to 1.9 GHz with steps of 0.1 GHz. The imaged surfaces are with radii of $r_1 = 50$ mm, $r_2 = 35$ mm, and $r_3 = 20$ mm.

In the first example, the two OUTs are placed at the cylindrical coordinates (r, ϕ, z) of (20 mm, $-170°$, 0) and (20 mm, 0°, 0). The container with OUTs is scanned along z while the antenna arrays are stationary. Scanning along z is performed from -2λ to 2λ with 21 sampling steps, where λ is the wavelength at the center frequency of 1.7 GHz for the used mixture.

To obtain the complex-valued scattered response R, for each receiver antenna, we combine the real and imaginary parts obtained from the in-phase (I) and quadrature (Q) channels of the quadrature receiver unit as $R = I + jQ$. The recorded complex-valued response for each receiver at angular position $\phi_{k'}$, longitudinal position z_l, and frequency ω_{n_f} is denoted by $R(\phi_{k'}, z_l, \omega_{n_f})$. At each acquisition, by default, the receiver unit provides 1024 samples over time for each channel. Since it is a direct conversion receiver with the frequency of the LO and RF signals being the same, we take average of these 1024 samples for each channel to obtain I and Q values.

PSFs are collected using small copper-coated plastic cylinders as COs. These COs have diameter of 18 mm and height of 10 mm and are placed, one at a time, at the cylindrical coordinates $(r_j, 0°, 0)$, $r_j = 50$, 35, and 20 mm.

To eliminate the effect of the background medium and the slight differences between the receiver antennas, it is necessary to implement a two-step calibration process. In the first step, we calibrate out the effect of the differences between the receiver antennas for each transmitting antenna a_m by dividing the responses $R_{a_m}(\phi_{k'}, z_l, \omega_{n_f})$, by the magnitude of the responses collected at a longitudinal position z_0 far away from the OUTs $|R_{a_m}(\phi_{k'}, z_0, \omega_{n_f})|$ as

$$R^1_{a_m}(\phi_{k'}, z_l, \omega_{n_f}) = R_{a_m}(\phi_{k'}, z_l, \omega_{n_f}) / \left| R_{a_m}(\phi_{k'}, z_0, \omega_{n_f}) \right|. \quad (17)$$

In the second step of the calibration process, to eliminate the effects of the background media (liquid, container, and any object other than OUTs), we calibrate each $R^1_{a_m}(\phi_{k'}, z_l, \omega_{n_f})$ response as

$$R^2_{a_m}(\phi_{k'}, z_l, \omega_{n_f}) = R^1_{a_m}(\phi_{k'}, z_l, \omega_{n_f}) - \bar{R}^1_{a_m}(\phi_{k'}, z_l, \omega_{n_f}) \quad (18)$$

where $\bar{R}^1_{a_m}(\phi_{k'}, z_l, \omega_{n_f})$ is the background response without the presence of the OUTs. In practice, $\bar{R}^1_{a_m}(\phi_{k'}, z_l, \omega_{n_f})$ can be the response at a longitudinal position z_0 far away from the OUTs. The two-step calibration process is applied on all the collected PSFs and OUT responses.

After collecting the PSFs and OUT responses and implementing the two-step calibration process, the three image reconstruction methods discussed in Section II are applied. The number of samples after interpolation along the azimuthal direction is 144 in all methods. Fig. 13 shows the reconstructed images obtained from the three methods. It is observed that Methods 1 and 2 provide images with similar quality in which the objects can be reconstructed well over the inner surface with some shadows observed over the middle and outer surfaces. The reconstructed image obtained from Method 3, however, only provides the correct radial location of the objects but fails to provide satisfactory image of the objects over the cross-range directions. Besides, images in Fig. 13(a) have lower quality compared with those in Fig. 7(a) (simulation example). The differences between the simulation and measured results are mainly due to the following factors: 1) the exact properties of the microwave absorbing sheets are not available. In the simulation, we used approximate electrical property values for carbon fiber absorbers found in the literature (see [40], [41]); 2) the exact models of the

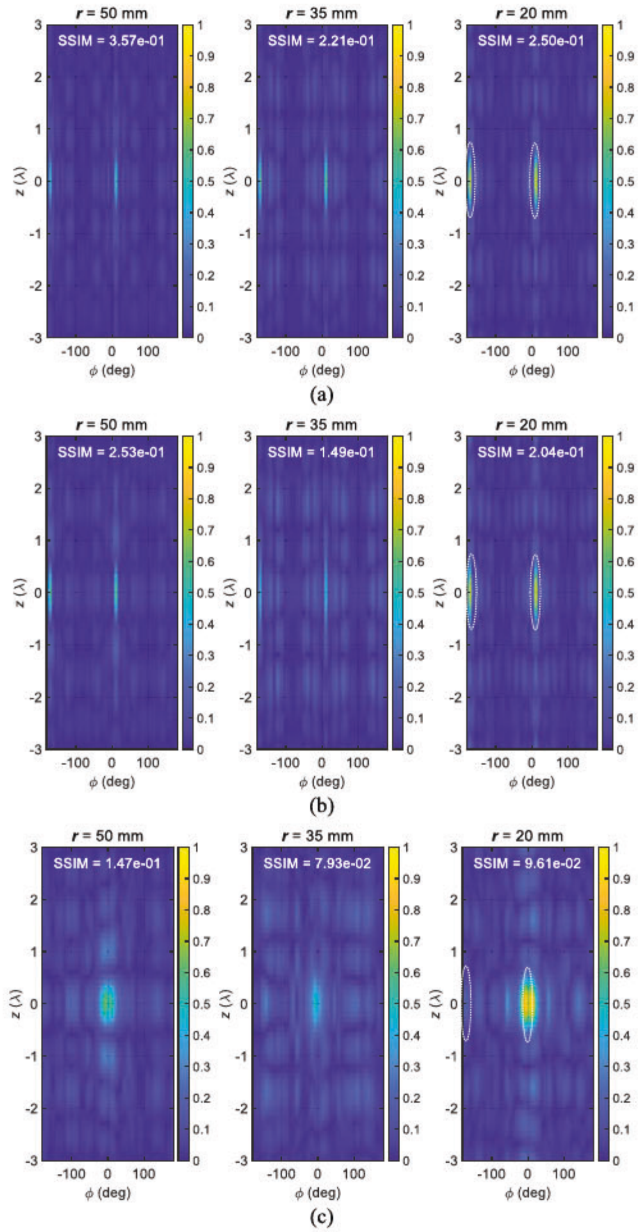

Fig. 13. Normalized images for two OUTs placed on the inner surface when using (a) Method 1, (b) Method 2, and (c) Method 3. White dotted lines show the true positions of the objects.

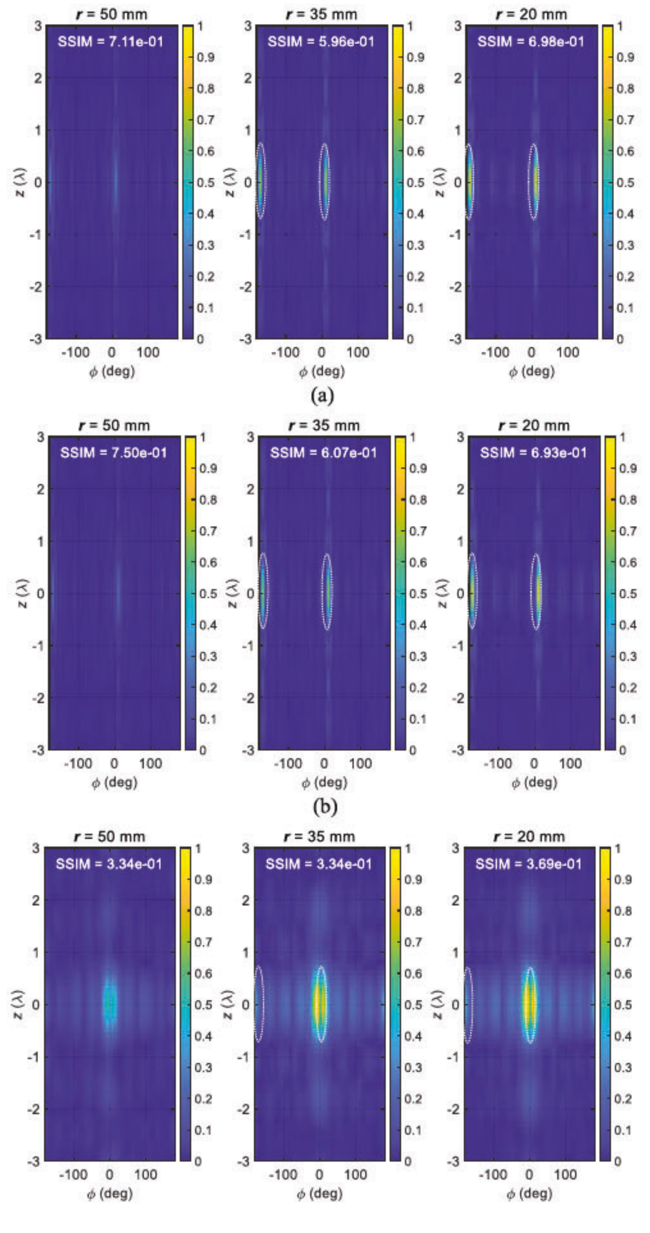

Fig. 14. Normalized images for two OUTs placed in between the middle and inner surfaces when using (a) Method 1, (b) Method 2, and (c) Method 3. White dotted lines show the true positions of the objects.

used commercial antennas are not available. In the simulation model, we used resonant dipole antennas; and 3) for affordable simulations, we did not include the 3-D printed antenna holder in the simulation model.

In the second example, the two OUTs are placed in the same ϕ and z positions as in the first example but approximately at midway between the inner and middle imaged surfaces along the radial direction. They are scanned with the same sampling parameters described for the first example. After similar processing discussed for the first example, Fig. 14 shows the reconstructed images obtained from the three methods. Again, it is observed that Methods 1 and 2 provide images with similar quality in which the objects can be reconstructed well over the inner and middle surfaces with some weak shadows observed over the outer surface. The reconstructed image obtained from Method 3; however, only provides the correct radial location of the objects (over the middle and inner surfaces) but fails to provide satisfactory images over cross-range directions.

VI. Conclusion and Discussion

In this article, a cylindrical holographic near-field 3-D imaging system was proposed based on the use of arrays of antennas along the azimuthal direction, three imaging methods, and the use of a low-cost, compact, and narrowband data acquisition system. The use of antenna arrays expedites the data acquisition but leads to limited and nonuniform samples along the azimuthal direction which necessitates introducing adequate processing techniques. Among the studied methods, the best performance was achieved when the samples are interpolated along the azimuthal direction prior to applying DFT.

It was observed that the use of the sLORETA and eLORETA approaches leads to the reconstruction of images with similar quality. However, the eLORETA approach requires more computational time mainly due to the use of an iterative algorithm to find the diagonal weights $\underline{\underline{\mathbf{W}}}$. For example, for the first simulation example in Section III-A, the time required to solve each system of equations is 30 ms for eLORETA and 3 ms for sLORETA on a Laptop computer with Intel i7-6820HQ 2.7 GHz CPU with 8 GB of RAM.

Most of the microwave imaging setups reported so far use VNAs for data acquisition. The common method for vector measurements in VNAs is the heterodyne architecture which is mature and accurate. However, the need for a less-expensive vector measurement system has been noticed by many researchers and solutions are emerging based on direct detection (homodyne) to reduce cost, components count, and power consumption (see [42], [43]). It has been shown that with the new commercial chips, direct detection systems can compete with a VNA in terms of accuracy [43]. The data acquisition system proposed in this work is along these efforts. Besides, such system provides further degrees of freedom in the selection of the desired frequency band, transmitter and receiver gains, and other important parameters compared with other commercial solutions such as software-defined radio (SDR) boards (see [44]). Overall, the use of low-cost off-the-shelf components for the data acquisition system allows for using that in various industrial settings.

In this work, the transmitter antennas do not operate as receivers. Using them as receivers allows for increasing the number of samples along the azimuthal direction and hence improving the quality of the images. However, this implies the use of additional hardware components (using circulators to transmit and receive simultaneously or using additional switches to receive responses by inactive transmitters).

A valid concern is that the LSI assumption used in this work may not hold for realistic imaging systems. According to the Born approximation, linearity of the system implies that the imaged objects should be small and low-contrast. However, such objects may provide weaker scattered responses that can be hardly measured. Thus, in practice, compromises need to be considered for obtaining satisfactory results. For instance, the security screening systems at the airports (see [3], [4]) assume linearity of the system while, obviously, this does not hold for large metallic objects such as guns. But those techniques can still provide satisfactory qualitative images of such objects. Space-invariant property also does not hold in a practical system but measurements over sufficiently long apertures and proper calibration schemes can still lead to satisfactory results (see [19]–[27]).

The sampling requirements and the resolution limits for a far-field SAR-based holographic imaging system have already been presented before (see [3], [4], [45]). Here, our setup is a near-field system in which the variations in the fields depend on the antennas and the shape and electrical properties of the media around them. Thus, it is not feasible to provide theoretical expressions for the resolution and sampling criteria addressing all possible scenarios. Overall, the sampling steps should be smaller than those in [4] and the chosen steps should be first validated by imaging of known OUTs for a given near-field imaging setup. Besides, one can expect to obtain better resolution limits in a near-field imaging system due to the measurement and processing of the evanescent waves.

APPENDIX A

Let us assume the function $f(\phi_n)$ has samples at angles ϕ_n, $n = 0, \ldots, N-1$, which are nonuniformly distributed along the ϕ-direction. The NUDFT of this function $\tilde{F}(k)$ can be written as

$$\tilde{F}(k) = \sum_{n=0}^{N-1} f(\phi_n) e^{-i2\pi(\phi_n/L_\phi)k} \tag{19}$$

where L_ϕ is the range of variation for the samples. If the samples are collected over a full circle, then $L_\phi = 2\pi$. Unlike inverse DFT, inverse NUDFT cannot be obtained just by changing $-i$ to i. Instead, it has to be computed from

$$\underline{f} = \underline{\underline{D}}^{-1}\underline{\tilde{F}} \tag{20}$$

where

$$\underline{f} = \begin{bmatrix} f(\phi_0) \\ \vdots \\ f(\phi_{N-1}) \end{bmatrix},$$

$$\underline{\underline{D}} = \begin{bmatrix} e^{-i2\pi(\phi_1/L_\phi)1} & \cdots & e^{-i2\pi(\phi_{N-1}/L_\phi)1} \\ \vdots & \ddots & \vdots \\ e^{-i2\pi(\phi_1/L_\phi)(N-1)} & \cdots & e^{-i2\pi(\phi_{N-1}/L_\phi)(N-1)} \end{bmatrix} \tag{21}$$

and

$$\underline{\tilde{F}} = \begin{bmatrix} \tilde{F}(0) \\ \vdots \\ \tilde{F}(N-1) \end{bmatrix}. \tag{22}$$

APPENDIX B

Suppose that x and y are two generic 2-D images that we would like to assess their similarity. According to [38], the SSIM is computed using three terms, namely, the luminance term $l(x, y)$, the contrast term $c(x, y)$, and the structural term $s(x, y)$ as

$$\text{SSIM}(x, y) = [l(x, y)]^\alpha [c(x, y)]^\beta [s(x, y)]^\gamma \tag{23}$$

$$l(x, y) = \frac{2\mu_x\mu_y + C_1}{\mu_x^2 + \mu_y^2 + C_1} \tag{24}$$

$$c(x, y) = \frac{2\sigma_x\sigma_y + C_2}{\sigma_x^2 + \sigma_y^2 + C_2} \tag{25}$$

$$s(x, y) = \frac{\sigma_{xy} + C_3}{\sigma_x\sigma_y + C_3} \tag{26}$$

where μ_x, μ_y, σ_x, σ_y, and σ_{xy} are the means, standard deviations, and cross-covariance for the images, respectively, C_1, C_2, and C_3 are constants determined based on the dynamic range of the pixel values [38], and α, β, and γ are used to adjust the importance of the terms (here, $\alpha = \beta = \gamma = 1$).

REFERENCES

[1] R. Appleby and H. B. Wallace, "Standoff detection of weapons and contraband in the 100 GHz to 1 THz region," *IEEE Trans. Antennas Propag.*, vol. 55, no. 11, pp. 2944–2956, Nov. 2007.

[2] M. C. Kemp, "Millimetre wave and terahertz technology for the detection of concealed threats—A review," *Proc. SPIE*, vol. 6402, pp. 1–2, Sep. 2006.

[3] D. M. Sheen, D. L. Mcmakin, and T. E. Hall, "Three-dimensional millimeter-wave imaging for concealed weapon detection," *IEEE Trans. Microw. Theory Techn.*, vol. 49, no. 9, pp. 1581–1592, Sep. 2001.

[4] D. Sheen, D. Mcmakin, and T. Hall, "Near-field three-dimensional radar imaging techniques and applications," *Appl. Opt.*, vol. 49, no. 19, p. E83, Jun. 2010.

[5] R. Zoughi, *Microwave Non-Destructive Testing and Evaluation*. Norwell, MA, USA: Kluwer, 2000.

[6] S. Kharkovsky and R. Zoughi, "Microwave and millimeter wave nondestructive testing and evaluation–overview and recent advances," *IEEE Instrum. Meas. Mag.*, vol. 10, no. 2, pp. 26–38, Apr. 2007.

[7] N. K. Nikolova, "Microwave near-field imaging of human tissue and its applications to breast cancer detection," *IEEE Microw. Mag.*, vol. 12, no. 7, pp. 78–94, Dec. 2011.

[8] R. Chandra, H. Zhou, I. Balasingham, and R. M. Narayanan, "On the opportunities and challenges in microwave medical sensing and imaging," *IEEE Trans. Biomed. Eng.*, vol. 62, no. 7, pp. 1667–1682, Jul. 2015.

[9] J. De Zaeytijd, A. Franchois, C. Eyraud, and J.-M. Geffrin, "Full-wave three-dimensional microwave imaging with a regularized gauss–Newton method—Theory and experiment," *IEEE Trans. Antennas Propag.*, vol. 55, no. 11, pp. 3279–3292, Nov. 2007.

[10] L. Liu, A. Trehan, and N. K. Nikolova, "Near-field detection at microwave frequencies based on self-adjoint response sensitivity analysis," *Inverse Prob.*, vol. 26, no. 10, pp. 1–28, Aug. 2010.

[11] Y. Zhang, S. Tu, R. K. Amineh, and N. K. Nikolova, "Resolution and robustness to noise of the sensitivity-based method for microwave imaging with data acquired on cylindrical surfaces," *Inverse Prob.*, vol. 28, no. 11, pp. 1–15, Oct. 2012.

[12] E. C. Fear, X. Li, S. C. Hagness, and M. A. Stuchly, "Confocal microwave imaging for breast cancer detection: Localization of tumors in three dimensions," *IEEE Trans. Biomed. Eng.*, vol. 49, no. 8, pp. 812–822, Aug. 2002.

[13] H. B. Lim, N. T. T. Nhung, E.-P. Li, and N. D. Thang, "Confocal microwave imaging for breast cancer detection: Delay-multiply-and-sum image reconstruction algorithm," *IEEE Trans. Biomed. Eng.*, vol. 55, no. 6, pp. 1697–1704, Jun. 2008.

[14] P. Corredoura, Z. Baharav, B. Taber, and G. Lee, "Millimeter-wave imaging system for personnel screening: Scanning 10^7 points a second and using no moving parts," *Proc. SPIE*, vol. 6211, May 2006, Art. no. 62110B.

[15] S. Ahmed, A. Schiessl, F. Gumbmann, M. Tiebout, S. Methfessel, and L.-P. Schmidt, "Advanced microwave imaging," *IEEE Microw. Mag.*, vol. 13, no. 6, pp. 26–43, Sep. 2012.

[16] Y.-K. Zhu, M.-H. Yang, L. Wu, Y. Sun, and X.-W. Sun, "Millimeter-wave holographic imaging algorithm with amplitude corrections," *Prog. Electromagn. Res. M*, vol. 49, pp. 33–39, Jul. 2016.

[17] R. K. Amineh, N. K. Nikolova, and M. Ravan, *Real-Time Three-Dimensional Imaging of Dielectric Bodies Using Microwave/Millimeter Wave Holography*. Hoboken, NJ, USA: Wiley, 2019.

[18] A. Zhuravlev, S. Ivashov, V. Razevig, I. Vasiliev, and T. Bechtel, "Shallow depth subsurface imaging with microwave holography," in *Proc. 19th Detection Sens. Mines, Explosive Objects, Obscured Targets*, Baltimore, MD, USA, vol. 9072, May 2014, Art. no. 90720X.

[19] R. K. Amineh, M. Ravan, A. Khalatpour, and N. K. Nikolova, "Three-dimensional near-field microwave holography using reflected and transmitted signals," *IEEE Trans. Antennas Propag.*, vol. 59, no. 12, pp. 4777–4789, Dec. 2011.

[20] R. K. Amineh, M. Ravan, R. Sharma, and S. Baua, "Three-dimensional holographic imaging using single frequency microwave data," *Int. J. Antennas Propag.*, vol. 2018, pp. 1–14, Jul. 2018.

[21] H. Wu and R. K. Amineh, "A low-cost and compact three-dimensional microwave holographic imaging system," *Electronics*, vol. 8, no. 9, p. 1036, Sep. 2019.

[22] H. Wu, M. Ravan, R. Sharma, J. Patel, and R. K. Amineh, "Microwave holographic imaging of nonmetallic concentric pipes," *IEEE Trans. Instrum. Meas.*, vol. 69, no. 10, pp. 7594–7605, Oct. 2020.

[23] R. K. Amineh, J. J. McCombe, A. Khalatpour, and N. K. Nikolova, "Microwave holography using point-spread functions measured with calibration objects," *IEEE Trans. Instrum. Meas.*, vol. 64, no. 2, pp. 403–417, Feb. 2015.

[24] R. K. Amineh, M. Ravan, J. McCombe, and N. K. Nikolova, "Three-dimensional microwave holographic imaging employing forward-scattered waves only," *Int. J. Antennas Propag.*, vol. 2013, pp. 1–15, 2013. 897287

[25] H. Wu, R. K. Amineh, and M. Ravan, "Near-field holographic microwave imaging using data collected over cylindrical apertures," in *Proc. 18th Int. Symp. Antenna Technol. Appl. Electromagn. (ANTEM)*, Aug. 2018, pp. 1–2.

[26] R. K. Amineh, M. Ravan, H. Wu, and A. Kasturi, "Three-dimensional holographic imaging using data collected over cylindrical apertures," *Microw. Opt. Technol. Lett.*, vol. 61, no. 4, pp. 907–911, Apr. 2019.

[27] R. K. Amineh, M. Ravan, and R. Sharma, "Nondestructive testing of nonmetallic pipes using wideband microwave measurements," *IEEE Trans. Microw. Theory Techn.*, vol. 68, no. 5, pp. 1763–1772, May 2020.

[28] D. Sheen, D. McMakin, and T. E. Hall, "Cylindrical millimeter-wave imaging technique for concealed weapon detection," *Proc. SPIE, Int. Soc. Opt. Eng.*, vol. 3240, pp. 242–250, Mar. 1998.

[29] D. M. Sheen, "Sparse multi-static arrays for near-field millimeter-wave imaging," in *Proc. IEEE Global Conf. Signal Inf. Process.*, Dec. 2013, pp. 699–702.

[30] M. T. Ghasr, M. J. Horst, M. R. Dvorsky, and R. Zoughi, "Wideband microwave camera for real-time 3-D imaging," *IEEE Trans. Antennas Propag.*, vol. 65, no. 1, pp. 258–268, Jan. 2017.

[31] S. S. Ahmed, A. Genghammer, A. Schiessl, and L.-P. Schmidt, "Fully electronic E-band personnel imager of 2 m^2 aperture based on a multistatic architecture," *IEEE Trans. Microw. Theory Techn.*, vol. 61, no. 1, pp. 651–657, Jan. 2013.

[32] M. T. Ghasr, M. A. Abou-Khousa, S. Kharkovsky, R. Zoughi, and D. Pommerenke, "Portable real-time microwave camera at 24 GHz," *IEEE Trans. Antennas Propag.*, vol. 60, no. 2, pp. 1114–1125, Feb. 2012.

[33] J. C. Bolomey and F. E. Gardiol, *Engineering Applications of the Modulated Scattering Technique*. Norwood, MA, USA: Artech House, 2001.

[34] R. D. Pascual-Marqui, "Standardized low-resolution brain electromagnetic tomography (sLORETA): Technical details," *Methods Find. Express Clin. Pharmacol.*, vol. 24, pp. 1–16, Jan. 2002.

[35] R. D. Pascual-Marqui, "Discrete, 3D distributed, linear imaging methods of electric neuronal activity. Part 1: Exact, zero error localization," 2007, *arXiv:0710.3341*. [Online]. Available: http://arxiv.org/abs/0710.3341

[36] D. Garcia, "Robust smoothing of gridded data in one and higher dimensions with missing values," *Comput. Statist. Data Anal.*, vol. 54, no. 4, pp. 1167–1178, Apr. 2010.

[37] R. D. Pascual-Marqui, "Review of methods for solving the EEG inverse problem," *Int. J. Bioelectromagnetism (IJBEM)*, vol. 1, pp. 75–86, Jan. 1999.

[38] Z. Wang, A. C. Bovik, H. R. Sheikh, and E. P. Simoncelli, "Image quality assessment: From error visibility to structural similarity," *IEEE Trans. Image Process.*, vol. 13, no. 4, pp. 600–612, Apr. 2004.

[39] P. M. Meaney, C. J. Fox, S. D. Geimer, and K. D. Paulsen, "Electrical characterization of glycerin: Water mixtures: Implications for use as a coupling medium in microwave tomography," *IEEE Trans. Microw. Theory Techn.*, vol. 65, no. 5, pp. 1471–1478, May 2017.

[40] S. Gona, P. Tomasek, and V. Kresalek, "Measurement of conductivity of carbon fibers at microwave frequencies," in *Proc. 23th Conf. Radioelektronika*, Pardubice, Czech Republic, 2013, pp. 68–71.

[41] A. Mehdipour, C. W. Trueman, A. R. Sebak, and S. V. Hoa, "Carbon-fiber composite T-match folded bow-tie antenna for RFID applications," in *Proc. IEEE Antennas Propag. Soc. Int. Symp.*, Charleston, SC, USA, Jun. 2009, pp. 1–4.

[42] N. Suwan, "Investigation of RF direct detection architecture circuits for metamaterial sensor applications," M.S. thesis, Dept. Elect. Comput. Eng., Univ. Waterloo, Waterloo, ON, Canada, 2011.

[43] D. J. Pagliari *et al.*, "A low-cost, fast, and accurate microwave imaging system for breast cancer detection," in *Proc. IEEE Biomed. Circuits Syst. Conf. (BioCAS)*, Oct. 2015, pp. 1–4.

[44] J. Marimuthu, K. S. Bialkowski, and A. M. Abbosh, "Software-defined radar for medical imaging," *IEEE Trans. Microw. Theory Techn.*, vol. 64, no. 2, pp. 643–652, Feb. 2016.

[45] M. Zhou, Y. Alfadhl, and X. Chen, "Optimal spatial sampling criterion in a 2D THz holographic imaging system," *IEEE Access*, vol. 6, pp. 8173–8177, 2018.

Hailun Wu (Member, IEEE) received the B.Eng. degree in opto-electronics engineering from Shenzhen University, Shenzhen, China, in 2017, and the M.Sc. degree (distinction) in electrical and computer engineering from New York Tech, New York, NY, USA, in 2019.

She has been a Research Assistant with the Applied Electromagnetics Research Laboratory, New York Tech, since 2017. Her research interests include microwave holographic imaging techniques, nondestructive testing, image reconstruction, microwave imaging systems, and RF and microwave circuit design.

Maryam Ravan (Senior Member, IEEE) received the Ph.D. degree from the Amirkabir University of Technology, Tehran, Iran.

She was a Post-Doctoral Fellow with the Departments of Electrical and Computer Engineering, University of Toronto, Toronto, ON, Canada, McMaster University, Hamilton, ON, and Ryerson University, Toronto, from May 2007 to April 2013, where she was involved in solving forward modeling and inverse problems and the related signal/image processing techniques for biomedical, radar systems, microwave imaging, and nondestructive testing (NDT) applications. She was also a Lecturer with the School of Computational Engineering and Science, McMaster University, from 2009 to 2012. From May 2013 to August 2017, she was a Senior Research Scientist with the Department of Research and Development, LivaNova PLC, London, U.K., where her work focused on developing quantitative biomarkers and machine learning algorithms for investigating the efficacy of closed-loop Vagus nerve stimulation (VNS) therapy for epilepsy. She is currently an Assistant Professor with the Department of Electrical and Computer Engineering, New York Institute of Technology, New York, NY, USA. She has authored or coauthored more than 70 journal and conference articles, a book chapter, and a book. Her research interests include signal and image processing, beamforming, machine learning, microwave holography, MIMO radar systems and space time adaptive processing, and nondestructive testing. Her research has been supported by U.S. National Science Foundation (NSF), DND/NSERC Research Partnership Grant with Defense Research and Development Canada (DRDC) and Raytheon Canada, Ltd., MITACS Internship with St. Joseph's Hospital in Hamilton, Canada, and NSERC Engage Grant with Raytheon Canada, Ltd.

Reza K. Amineh (Senior Member, IEEE) received the Ph.D. degree in electrical engineering from McMaster University, Hamilton, ON, Canada, in 2010.

He was a Principal Scientist with the Department of Sensor Physics, Halliburton Co., Houston, TX, USA, from 2013 to 2016. He was a Post-Doctoral Fellow at the University of Toronto, Toronto, ON, and McMaster University, from 2012 to 2013 and from 2010 to 2012, respectively. He was a Ph.D. Intern with the Advanced Technology Group, BlackBerry, Waterloo, ON, in 2009. He is currently an Assistant Professor with the Department of Electrical and Computer Engineering, New York Institute of Technology, New York, NY, USA. He has authored or coauthored more than 75 journal and conference articles, two book chapters, and a book titled *Real-Time Three-Dimensional Imaging of Dielectric Bodies Using Microwave/Millimeter Wave Holography* published by Wiley and IEEE Press. He contributed to more than 40 patent disclosures in applied electromagnetics while working at Halliburton Co and received several industrial awards. His research interests include applied electromagnetics with applications in imaging and sensing.

Dr. Amineh was a recipient of the Banting Post-Doctoral Fellowship from the Government of Canada in 2012 and the Ontario Ministry of Research and Innovation (OMRI) Post-Doctoral Fellowship in 2010. During his Ph.D. program, he was awarded the McMaster Internal Prestige Scholarship Clifton W. Sherman for two consecutive years. He has coauthored a paper selected as a finalist in the student paper competition at the IEEE Wireless and Microwave Technology Conference in 2019, an Honorable Mention Paper presented at the IEEE Symposium on Antennas and Propagation in 2008, and an article selected among the journal of *Inverse Problems' "Highlights Collection of 2010.*"